Aster Proteins Regulate the Accessible Cholesterol Pool in the Plasma Membrane

Alessandra Ferrari,[a] Cuiwen He,[b] John Paul Kennelly,[a] Jaspreet Sandhu,[a] Xu Xiao,[a] Xun Chi,[c] Haibo Jiang,[d] Stephen G. Young,[b] Peter Tontonoz[a]

aDepartment of Pathology and Laboratory Medicine and Department of Biological Chemistry, University of California, Los Angeles, California, USA
bDepartment of Medicine, Division of Cardiology and Department of Human Genetics, University of California, Los Angeles, California, USA
cDepartment of Microbiology, Immunology and Molecular Genetics, University of California, Los Angeles, California, USA
dSchool of Molecular Sciences, University of Western Australia, Perth, Australia

Alessandra Ferrari and Cuiwen He contributed equally to this article. (Order was determined randomly.)

ABSTRACT Recent studies have demonstrated the existence of a discrete pool of cholesterol in the plasma membranes (PM) of mammalian cells—referred to as the accessible cholesterol pool—that can be detected by the binding of modified versions of bacterial cytolysins (e.g., anthrolysin O). When the amount of accessible cholesterol in the PM exceeds a threshold level, the excess cholesterol moves to the endoplasmic reticulum (ER), where it regulates the SREBP2 pathway and undergoes esterification. We reported previously that the Aster/Gramd1 family of sterol transporters mediates nonvesicular movement of cholesterol from the PM to the ER in multiple mammalian cell types. Here, we investigated the PM pool of accessible cholesterol in cholesterol-loaded fibroblasts with a knockdown of Aster-A and in mouse macrophages from Aster-B and Aster-A/B-deficient mice. Nanoscale secondary ion mass spectrometry (NanoSIMS) analyses revealed expansion of the accessible cholesterol pool in cells lacking Aster expression. The increased accessible cholesterol pool in the PM was accompanied by reduced cholesterol movement to the ER, evidenced by increased expression of SREBP2-regulated genes. Cosedimentation experiments with liposomes revealed that the Aster-B GRAM domain binds to membranes in a cholesterol concentration-dependent manner and that the binding is facilitated by the presence of phosphatidylserine. These studies revealed that the Aster-mediated nonvesicular cholesterol transport pathway controls levels of accessible cholesterol in the PM, as well as the activity of the SREBP pathway.

Recent studies have demonstrated three functionally distinct pools of plasma membrane (PM) cholesterol (1). One pool, referred to as the "accessible cholesterol pool," expands when there is an excess of cholesterol in the PM. Cholesterol in the accessible pool is not sequestered by sphingomyelin or phospholipids. Accessible cholesterol can be detected and quantified experimentally by the binding of modified versions of bacterial cytolysins (e.g., domain 4 of anthrolysin O [ALO-D4]) (1, 2). A second pool of cholesterol is sequestered by sphingomyelin but can become accessible when sphingomyelin is cleaved with sphingomyelinase (SMase). The third pool has been deemed "essential" because its depletion impairs PM integrity and cell viability. Even after SMase treatment, the essential pool of cholesterol remains inaccessible to cholesterol-binding cytolysins.

Low-density lipoproteins (LDL) are internalized by endocytosis of LDL receptors and then traffic to lysosomes, where the cholesterol is liberated (3). Das et al. (1) demonstrated that cholesterol in lysosomes then moves to the PM, and only then, after expanding the accessible cholesterol pool in the PM, does cholesterol move to the

endoplasmic reticulum (ER). In this way, the PM is supplied with the cholesterol required for cell viability, and the ER is able to monitor PM cholesterol levels, ensuring optimal regulation of the SREBP2 pathway and cellular cholesterol homeostasis.
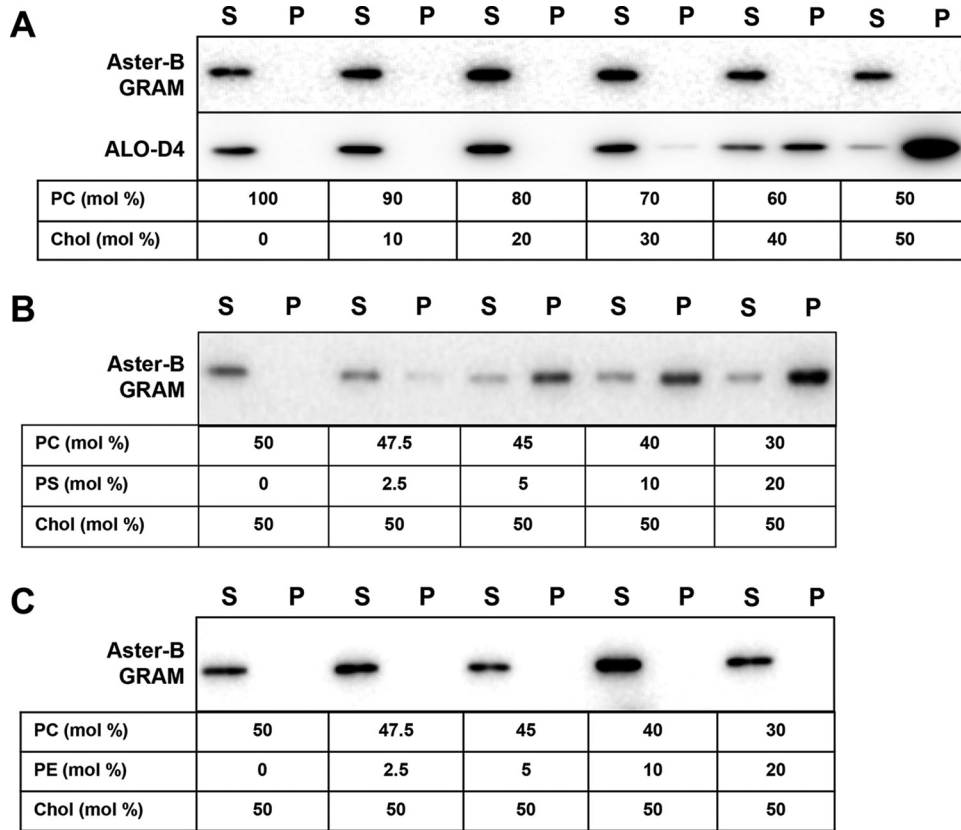
The ER forms membrane contacts with multiple organelles (4), and ER-PM contact sites have been proposed to facilitate nonvesicular transfer of lipids (5, 6). Recently, we characterized a family of ER-anchored cholesterol transporters called Asters that are expressed in most, if not all, mammalian cells (7). Aster-A, -B, and -C are encoded by the *Gramd1a*, *-b*, and *-c* genes in mice. Asters serve to remove excess PM cholesterol and redirect it, by nonvesicular transport, to the ER. The three Aster proteins appear to share a capacity for PM-to-ER transport of cholesterol, but each has a distinct tissue pattern of expression. We showed that Aster-B expression in the adrenal cortex is required for the movement of high-density lipoprotein (HDL)-derived cholesterol from the PM to the ER (7), but the physiological relevance of the other Aster proteins is currently unknown.

Earlier work showed that the GRAM domains of the Aster proteins are recruited to the PMs of living cells in response to cholesterol loading and facilitate the formation of PM-ER contacts, where sterol transfer occurs (7). Prior *in vitro* studies showed that the Aster GRAM domain binds anionic lipids, including phosphatidylserine (PS), suggesting that increased levels of PM cholesterol are sensed through a change in the presentation of phosphatidylserine (7, 8). Whether Asters recognize specific plasma cholesterol pools in the PMs of living cells and whether this function is tied to the regulation of ER processes remain to be clarified.

In the current study, we used nanoscale secondary ion mass spectrometry (NanoSIMS) combined with a ^{15}N-labeled ALO-D4 probe to visualize and quantify distributions of accessible cholesterol in the PM. This technology has been used previously to quantify PM accessible cholesterol in CHO-K1 cells (9) and in mouse peritoneal macrophages (10, 11). Our data demonstrate that Aster proteins regulate the PM accessible cholesterol pool by moving surplus cholesterol to the ER. When Aster protein expression is reduced, the PM accessible pool is expanded and the ER pool contracts, as evident from increased activity of SREBP-regulated genes. These findings highlight a mechanism that links PM cholesterol stores to the regulation of sterol homeostatic mechanisms in the ER.
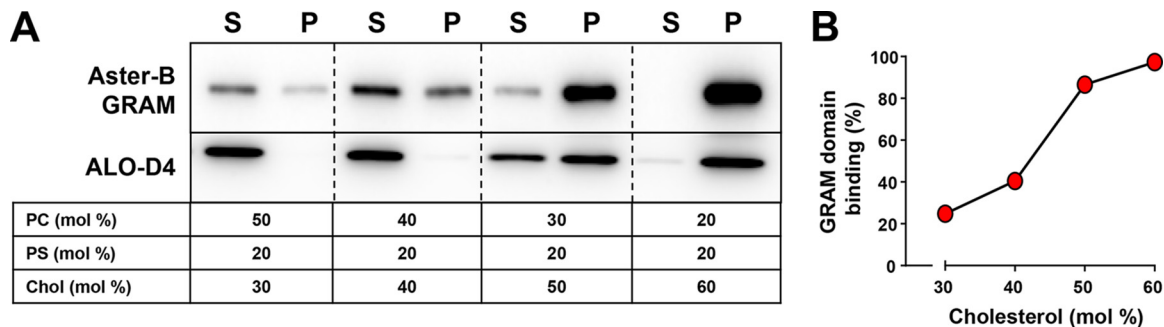
RESULTS

We originally showed that Aster proteins bind phosphatidylserine, which is abundant in the inner leaflet of the PM, and are recruited to the PM in living cells in a cholesterol concentration-dependent manner (7). To better understand interactions between the Aster GRAM domain and cholesterol- and phospholipid-containing membranes, we performed cosedimentation assays in which purified Aster-B GRAM domain was incubated with liposomes containing varying amounts of cholesterol and phospholipids. We used ALO-D4 binding as a control in these studies, based on the discovery, by Radhakrishnan and colleagues that ALO-D4 binds to cholesterol in phospholipid liposomes (12). In our current studies, we found that ALO-D4 could bind phosphatidylcholine (PC) liposomes containing 40% or more cholesterol (Fig. 1A). In contrast, the Aster-B GRAM domain did not bind pure PC liposomes containing up to 50% cholesterol. However, incorporating phosphatidylserine into the liposomes resulted in robust GRAM domain binding and did so in a concentration-dependent fashion (Fig. 1B). On the other hand, incorporation of phosphatidylethanolamine into the liposomes did not affect GRAM domain binding, providing further support for the specificity of Aster recruitment to membranes (Fig. 1C). Additional studies showed that the Aster-B GRAM domain was able to bind mixed phosphatidylcholine/phosphatidylserine liposomes containing 30% or more cholesterol (Fig. 2). These studies demonstrate that the Aster GRAM domain recognizes cholesterol in the presence of phosphatidylserine and support the notion that Aster proteins play a key role in regulating levels of accessible cholesterol in the PM. Our findings are consistent with the recently reported results of Naito et al., who used a similar approach to study Gramd1-liposome interactions (7, 8).

A

	S	P	S	P	S	P	S	P	S	P	S	P
Aster-B GRAM												
ALO-D4												

| PC (mol %) | 100 | | 90 | | 80 | | 70 | | 60 | | 50 | |
| Chol (mol %) | 0 | | 10 | | 20 | | 30 | | 40 | | 50 | |

B

	S	P	S	P	S	P	S	P	S	P
Aster-B GRAM										

PC (mol %)	50		47.5		45		40		30	
PS (mol %)	0		2.5		5		10		20	
Chol (mol %)	50		50		50		50		50	

C

	S	P	S	P	S	P	S	P	S	P
Aster-B GRAM										

| PC (mol %) | 50 | | 47.5 | | 45 | | 40 | | 30 | |
| PE (mol %) | 0 | | 2.5 | | 5 | | 10 | | 20 | |
| Chol (mol %) | 50 | | 50 | | 50 | | 50 | | 50 | |

FIG 1 Specificity of Aster-B GRAM domain interactions with artificial membranes. (A) Results of a cosedimentation assay testing the interaction of the Aster-B GRAM domain and ALO-D4 with liposomes containing cholesterol (Chol) and phosphatidylcholine. S, supernatant; P, pellet. (B) The Aster-B GRAM domain binds to phospholipid liposomes containing phosphatidylcholine, phosphatidylserine, and cholesterol. There was increased binding of the Aster-B GRAM domain to liposomes with increasing amounts of phosphatidylserine in liposomes. (C) The Aster-B GRAM domain does not bind to phospholipid liposomes containing phosphatidylcholine, phosphatidylethanolamine (PE), and cholesterol.

We previously used nanoscale secondary ion mass spectrometry (NanoSIMS) imaging to visualize and quantify the distribution of accessible cholesterol in the PMs of CHO cells (9) and macrophages (10, 11). Here, we adapted this approach to examine the influence of Aster protein deficiency on the PM pool of accessible cholesterol. In our first experiment, we used NanoSIMS to visualize and quantify binding of ^{15}N-labeled ALO-D4 to the PMs of 3T3-L1 preadipocytes. We were able to effectively knock down the expression of Aster-A, the main Aster family member in 3T3-L1 cells (7), with an

A

	S	P	S	P	S	P	S	P
Aster-B GRAM								
ALO-D4								

PC (mol %)	50		40		30		20	
PS (mol %)	20		20		20		20	
Chol (mol %)	30		40		50		60	

B

GRAM domain binding (%) vs Cholesterol (mol %): points at approximately (30, 25), (40, 40), (50, 87), (60, 97).

FIG 2 The Aster-B GRAM domain recognizes cholesterol in membranes containing phosphatidylserine. (A) Results of a cosedimentation assay showing increasing amounts of Aster-B GRAM domain in PC/PS-containing liposomes with increasing amounts of cholesterol. (B) Quantification of Aster-B binding from the study results in panel A.
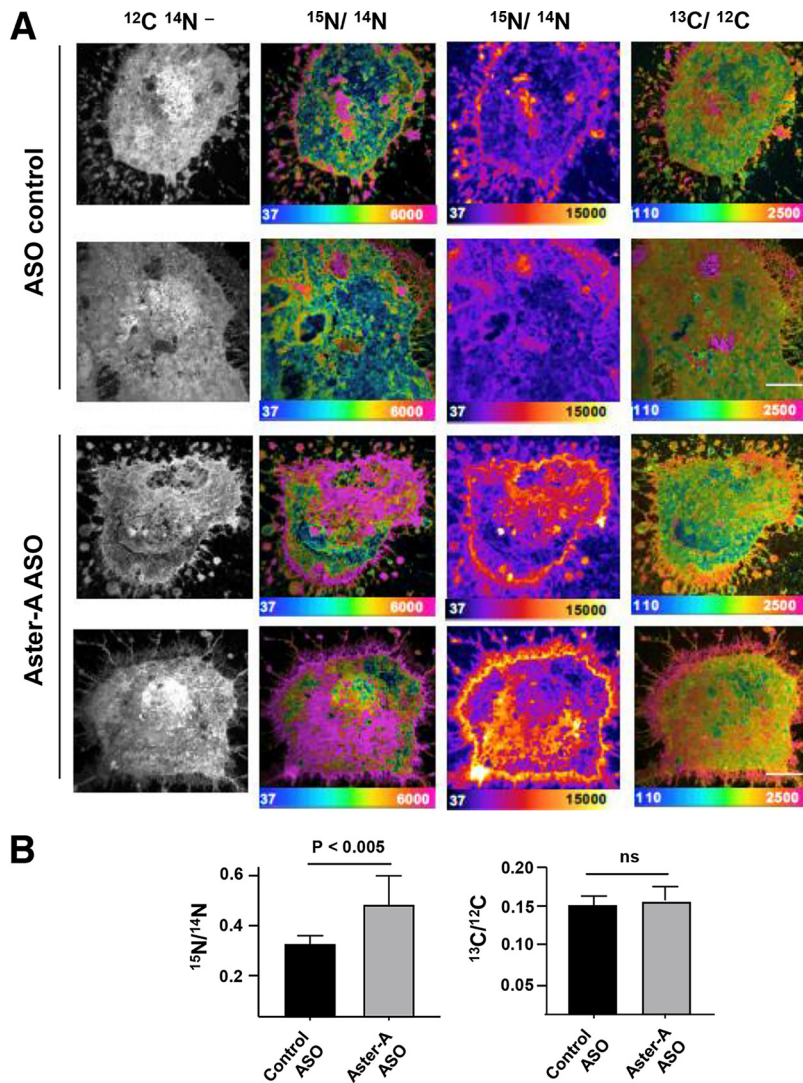
FIG 3 Deficiency of Aster-A in 3T3-L1 cells results in increased amounts of accessible cholesterol on the PM. 3T3-L1 cells were treated for 48 h with an Aster-A-specific ASO or a control ASO and then [^{13}C]cholesterol loaded by incubating with 50 μM MβCD-[^{13}C]cholesterol complexes for 3 h. Levels of accessible cholesterol in the fibroblast PM were assessed by measuring the binding of ^{15}N-labeled ALO-D4 to cells. (A) ^{15}N/^{14}N NanoSIMS images of fibroblasts revealing increased ^{15}N-labeled ALO-D4 binding to cells that had been treated with the Aster-A ASO. The ^{13}C/^{12}C NanoSIMS images show comparable levels of [^{13}C]cholesterol loading in cells regardless of whether they had been treated with the Aster-A-specific ASO or the control ASO. The ^{12}C^{14}N$^-$ images are useful for visualizing cell morphology. Scale bars, 10 μm. The ^{15}N/^{14}N and ^{13}C/^{12}C scales are multiplied by 10,000. (B) Quantification of NanoSIMS data from 5 fibroblasts treated with the control ASO and 9 fibroblasts treated with the Aster-A-specific ASO. The y axis in the ^{15}N/^{14}N bar graph starts at 0.0037 (^{15}N natural abundance); the y axis in the ^{13}C/^{12}C bar graph starts at 0.011 (^{13}C natural abundance). The data are presented as means and standard deviations (SD). ns, not significant. Differences were assessed with a Student t test with Welch's correction.

antisense oligonucleotide (ASO). 3T3-L1 cells treated with a control ASO or the Aster-A-specific ASO were plated on poly-D-lysine-coated silicon wafers and then [^{13}C]cholesterol loaded for 3 h with methyl-β-cyclodextrin (MβCD)-[^{13}C]cholesterol complexes. The cells were then incubated with ^{15}N-labeled ALO-D4 for 2 h at 4°C, washed, and processed for NanoSIMS analyses. The ^{12}C^{14}N$^-$ NanoSIMS images, reflecting the nitrogen content of the cells, were useful for visualizing cell morphology, and the ^{13}C/^{12}C NanoSIMS images confirmed that the cells had been loaded with [^{13}C]cholesterol (Fig. 3A). The amounts of [^{13}C]cholesterol in the PMs of fibroblasts treated with the control ASO or the Aster-A ASO were not different (Fig. 3B). Of note, however, the
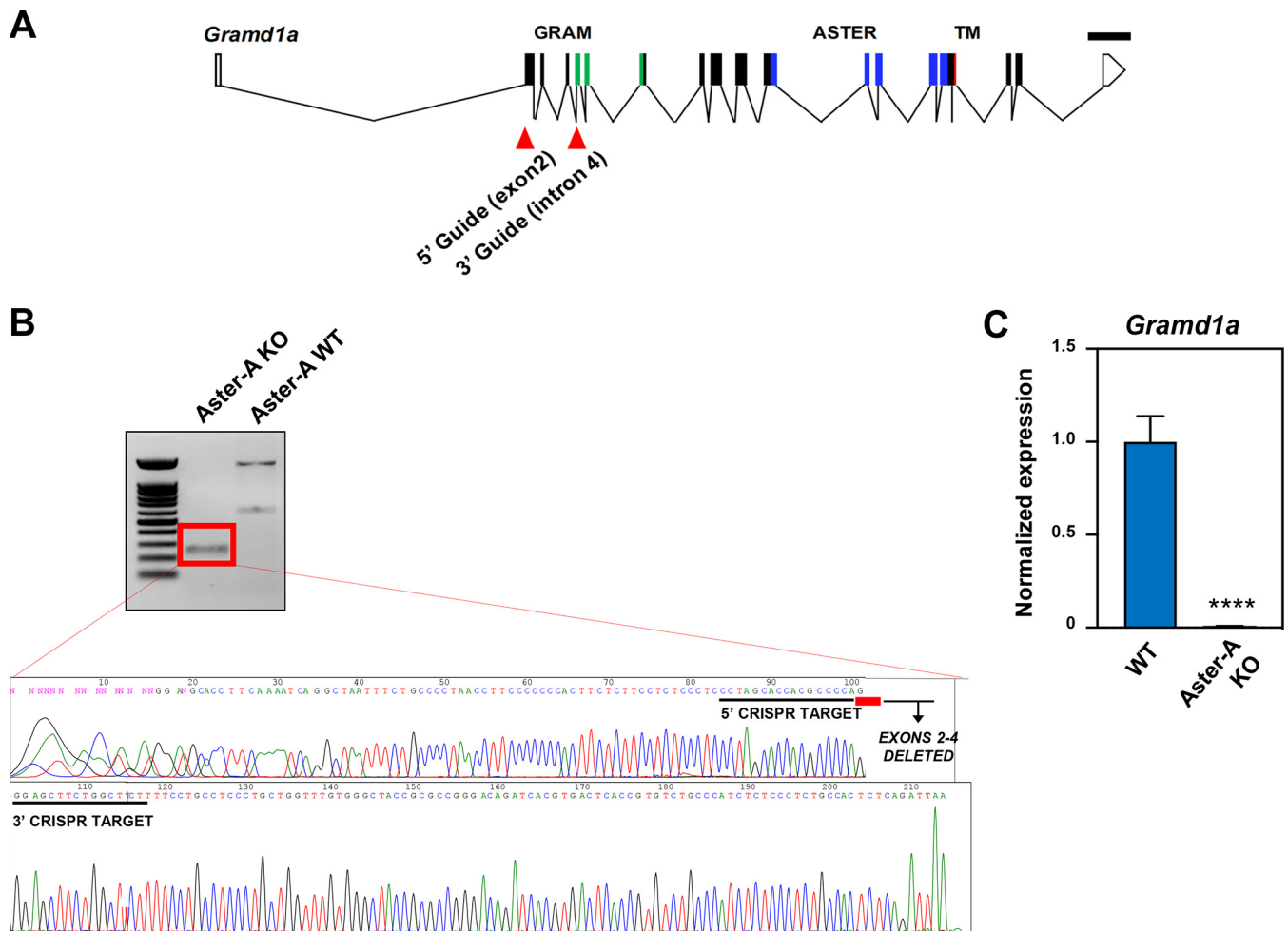
FIG 4 Generation of Aster-A knockout mice. (A) Strategy for generating *Gramd1a* (Aster-A) knockout mice by CRISPR-Cas9 genome editing. Coding exons are depicted in black. Exons that correspond to the GRAM domain, ASTER domain, and transmembrane (TM) domain are depicted in green, blue, and red, respectively. Scale bar, 1 kb. (B) Verification of the CRISPR-Cas9-induced mutation of Aster-A by PCR and DNA sequencing. The graph shows Sanger sequencing results of the band (boxed area) excised after amplification of DNA. The primers were designed to detect a 230-bp band in mice with deletion. Sequencing of the band confirmed the deletion; the red box in the graph indicates the deletion site, confirming that exons 2 to 4 were efficiently deleted. (C) Aster-A transcript levels by real-time quantitative reverse transcription (RT)-PCR. ****, $P < 0.0001$.

$^{15}N/^{14}N$ images revealed increased binding of ^{15}N-labeled ALO-D4 to the PMs of Aster-A-deficient cells, reflecting expansion of the accessible cholesterol pool (Fig. 2A). The $^{13}C/^{12}C$ ratio was ~55% higher in cells treated with Aster-A ASO than in cells treated with the control ASO (Fig. 3B).

To determine whether a knockout of Aster proteins affects the size of the PM accessible cholesterol pool, we analyzed primary mouse peritoneal macrophages from Aster-deficient mice. Macrophages can easily be loaded with cholesterol, because they express scavenger receptors that are not subject to feedback inhibition by cholesterol (13). For this reason, mouse peritoneal macrophages represent an ideal model for testing how Aster proteins affect levels of accessible cholesterol in the PM. We previously reported that *Gramd1b* (encoding Aster-B) is expressed at high levels in macrophages and that its expression is induced by an LXR agonist (7). *Gramd1a* (encoding Aster-A) is also expressed in murine macrophages. Earlier work demonstrated that all three members of the Aster family are capable of transferring cholesterol from the PM to the ER (7). We generated Aster-A knockout (KO) mice (Fig. 4A and B) and showed that Aster-A transcripts were absent from the peritoneal macrophages of these mice (Fig. 4C). We then intercrossed the Aster-A- and Aster-B-deficient mice to create mice lacking both Aster proteins.
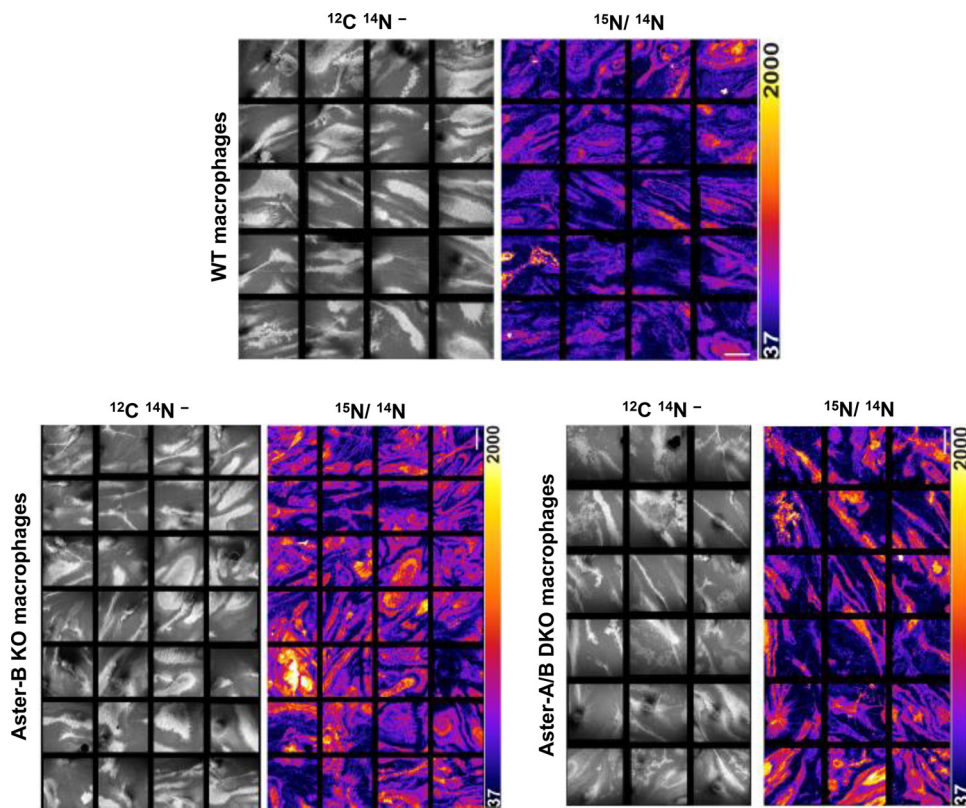
FIG 5 NanoSIMS images showing that Aster deficiency results in increased ^{15}N-labeled ALO-D4 binding to the plasma membranes of mouse peritoneal macrophages. Shown are NanoSIMS images of WT, Aster-B KO, and Aster-A/B DKO macrophages. The ^{12}C^{14}N$^-$ NanoSIMS images are useful for defining cell morphology; the ^{15}N/^{14}N NanoSIMS images depict binding of ^{15}N-labeled ALO-D4 to macrophages. Scale bars, 20 μm. The ^{15}N/^{14}N scale is multiplied by 10,000.

Macrophages from wild-type (WT) mice, Aster-B KO mice, and Aster-A/B double-knockout (DKO) mice were loaded with acetylated LDL (Ac-LDL) (50 μg/ml) for 48 h and then incubated with Alexa Fluor 594-conjugated ^{15}N-labeled ALO-D4 for 2 h at 4°C. Following fixation, the cells were processed for NanoSIMS analyses. NanoSIMS revealed higher levels of ^{15}N-labeled ALO-D4 binding to the peritoneal macrophages from Aster-B KO mice and Aster-A/B DKO mice, indicating an expanded pool of accessible cholesterol in the PM (Fig. 5 and 6). The ^{15}N/^{14}N ratio was ~45% higher in Aster-B KO and Aster-A/B DKO macrophages than in WT macrophages. Figure 5 shows images from multiple fields of cells of each genotype, revealing consistent differences in the levels of ^{15}N-labeled ALO-D4 binding. Figure 6 shows higher-magnification images of the macrophages from each genotype and quantification of ^{15}N-labeled ALO-D4 binding. Aster-B KO and Aster-A/B DKO macrophages had comparable levels of ^{15}N-labeled ALO-D4 binding.

To corroborate the NanoSIMS findings, we analyzed ALO-D4 binding by confocal microscopy. We observed increased binding of Alexa Fluor 594-conjugated ^{15}N-labeled ALO-D4 to the PMs of Aster-B KO and Aster-A/B DKO macrophages (Fig. 7A). Quantification of fluorescence intensities paralleled the NanoSIMS findings (Fig. 7B).

To investigate if the accumulation of accessible cholesterol in the PMs of Aster-deficient macrophages was associated with impaired movement of cholesterol to the ER, we analyzed the expression of SREBP2-regulated genes in WT, Aster-B KO, and Aster-A/B DKO macrophages in the settings of both cholesterol depletion and cholesterol loading (Fig. 8A). When macrophages were incubated in low-cholesterol medium containing 1% lipoprotein-deficient serum (LPDS), both Aster-B KO and Aster-A/B DKO macrophages exhibited increased expression of *Srebf2* and its target genes (*Hmgcs*,
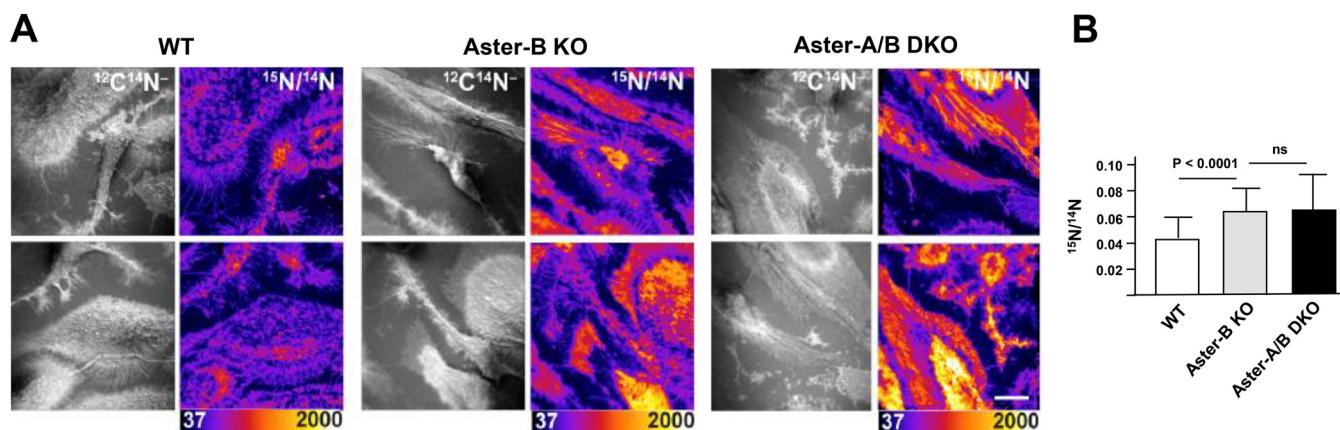
FIG 6 The accessible cholesterol pool in the PM is expanded in the setting of Aster deficiency. (A) $^{15}N/^{14}N$ NanoSIMS images reveal more ^{15}N-labeled ALO-D4 binding to Aster-B and Aster-A/B DKO macrophages than to WT macrophages. The $^{12}C^{14}N^-$ images are useful for defining cell morphology. Scale bar, 10 μm. The $^{15}N/^{14}N$ scale is multiplied by 10,000. (B) Quantification of $^{15}N/^{14}N$ ratios from WT ($n = 58$), Aster-B KO ($n = 268$), and Aster-A/B DKO ($n = 156$) macrophages, revealing ~45% greater ^{15}N enrichment in Aster-B KO and Aster-A/B DKO macrophages than in WT macrophages. The y axis in the $^{15}N/^{14}N$ bar graph starts at 0.0037 (^{15}N natural abundance). The data show means and SD. Differences were assessed with a Student's t test with Welch's correction. ns, not significant.

Hmgcr, *Sqle*, and *Ldlr*) (Fig. 8B and C). Concordant results were observed in Aster-A/B DKO macrophages that had been cholesterol loaded for 2 h with cyclodextrin-cholesterol complexes (Fig. 8D and E). Gene expression perturbations in cholesterol-loaded Aster-B KO macrophages followed the same trend, although the induction of SREBP2 target genes was more modest. Aster-B deletion, especially in the setting of sterol depletion, resulted in increased *Gramd1a* expression. Our findings support the conclusion that processing of SREBP2 increased in the absence of Aster proteins. Collectively, our studies indicate that the Aster proteins help to determine amounts of accessible cholesterol in the PM and that the accessible cholesterol pool size is linked to activation of the SREBP pathway in the ER.

DISCUSSION

Work over the past 5 years has highlighted the physiological importance of a pool of accessible cholesterol in the PM that expands in response to cholesterol loading (1, 2). Seminal studies by Das and coworkers (1) showed that when fibroblasts are incubated with LDL, the cholesterol moves first to lysosomes and subsequently to the PM, where it expands the accessible pool of cholesterol. Within minutes, this expanded pool of accessible cholesterol in the PM begins to contract, coinciding with transfer of cholesterol to the ER, where the cholesterol both regulates the activity of the SREBP
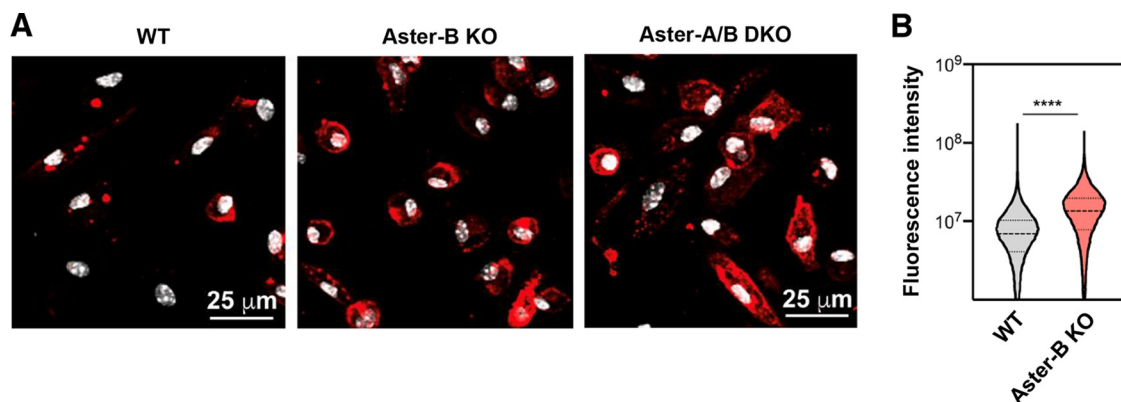
FIG 7 Loss of Aster-B in macrophages results in increased binding of Alexa Fluor 594-conjugated ^{15}N-labeled ALO-D4 to the plasma membrane. (A) Immunofluorescence microscopy images depicting the binding of Alexa Fluor 594-conjugated ALO-D4 (red) to macrophages. DNA was stained with DAPI (white). (B) Violin plot of fluorescence intensities in WT and Aster-B KO macrophages; 61,446 WT and 40,223 Aster-B KO cells were analyzed. ****, $P < 0.0001$.
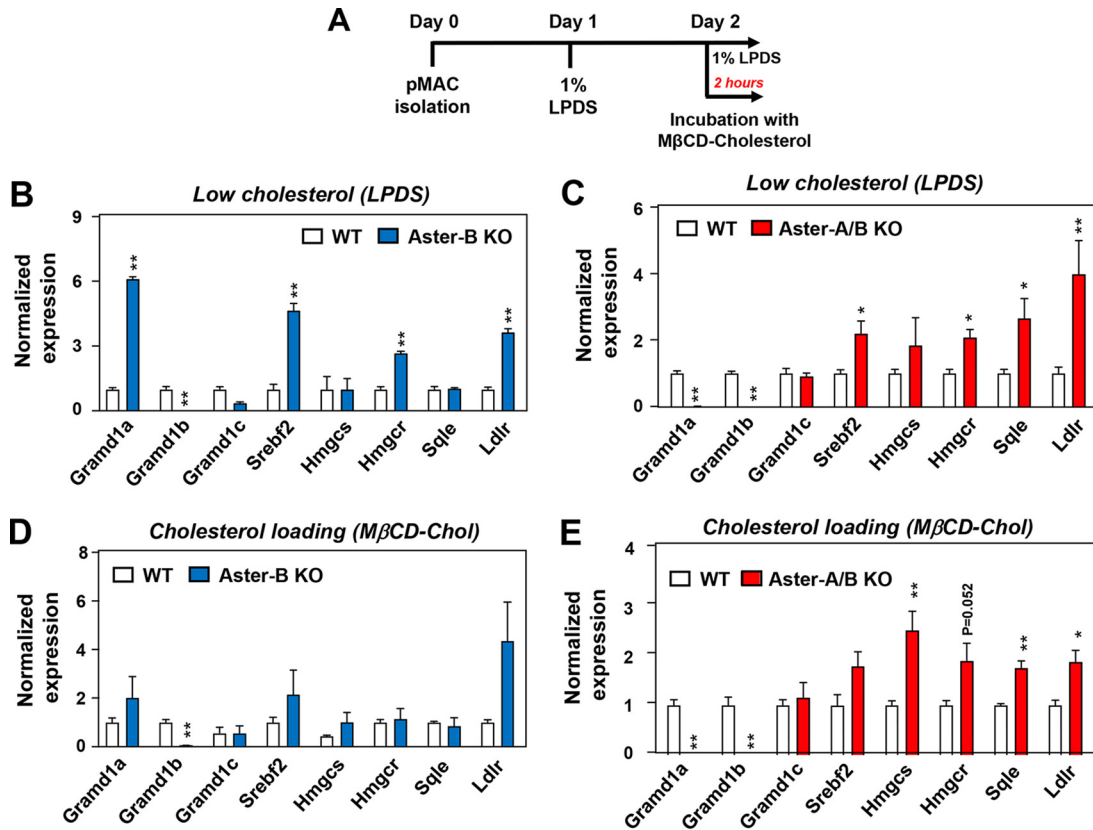
FIG 8 Inactivation of Aster genes activates the SREBP2 pathway. (A) Macrophages isolated from WT, Aster-B KO, and Aster-A/B DKO mice were cultured in 1% LPDS or were cholesterol loaded with 50 μM MβCD-cholesterol complexes. pMAC, peritoneal macrophage. (B to E) Real-time PCR analysis of gene expression in macrophages cultured in medium containing 1% LPDS and in macrophages that had been cholesterol loaded for 2 h with MβCD-cholesterol complexes. The data are presented as means and standard errors of the mean (SEM). Differences were assessed with one-way analysis of variance (ANOVA) with Dunnett *post hoc* tests. *, $P < 0.05$; **, $P < 0.01$.

transcription factors and undergoes esterification by acyl coenzyme A cholesterol acyltransferase (ACAT). This "cholesterol itinerary" within cells implied the existence of a physiological process for sensing surplus cholesterol in the PM and an efficient mechanism for moving it to the ER.

A leading candidate for an accessible cholesterol PM-to-ER transport mechanism is the Aster/Gramd1 family of mammalian nonvesicular transporters (7, 8). The Aster proteins (Aster-A, Aster-B, and Aster-C), which are integral membrane proteins of the ER, play an important role in detecting cholesterol in the PM and moving it to the ER (7). Aster proteins are recruited to the PM in response to cholesterol loading, creating PM-ER contacts that facilitate cholesterol transfer to the ER. We previously showed that one family member, Aster-B, is crucial for the transport of HDL-derived cholesterol from SR-B1 to the ER in the adrenal cortex. In adrenocortical cells, cholesterol in high-density lipoproteins moves into the PM, a process mediated by SR-B1. Aster-B mediates the next step, which is to move the surplus cholesterol in the PM to the ER. In the setting of SR-B1 or Aster-B deficiency, cholesterol delivery to the ER is markedly impaired, resulting in a striking reduction of cytosolic cholesterol ester droplets and defective synthesis of adrenocortical hormones (7). Aster-B is the predominant Aster family member in adrenocortical cells, but the other two Aster proteins have distinct tissue patterns of expression, and it is likely that they are involved in PM-to-ER cholesterol movement. At this point, however, our understanding of the role of the Aster proteins in controlling the dynamics of the accessible PM cholesterol pool in physiological contexts is limited.

In the current studies, we used ^{15}N-labeled ALO-D4 and NanoSIMS imaging to assess

the size of the PM accessible cholesterol pool in cholesterol-loaded control and Aster-deficient cells. Both an acute knockdown of Aster-A expression in 3T3-L1 fibroblasts with an ASO and the elimination of Aster-A and Aster-B gene expression in macrophages increased the size of the PM accessible cholesterol pool. The fact that we observed similar findings in different cell types and with different strategies for cholesterol loading (cyclodextrin-cholesterol complexes or Ac-LDL) strongly implied that Aster proteins are important for regulating the PM accessible cholesterol pool in many, if not all, cells. Our results also add to evidence indicating that the three different Aster proteins perform similar functions in regulating PM cholesterol levels, despite the fact that they have distinct patterns of expression and are regulated independently (7).

The experiments reported here focused on Aster-A and Aster-B, as they are highly expressed in the cell culture models that we examined. In 3T3-L1 fibroblasts, where Aster-A is most abundant, the knockdown was sufficient to modulate the pool of accessible cholesterol. In peritoneal macrophages, we detected high transcript levels for both Aster-A and Aster-B, but the absence of suitable antibodies precluded a comparison of their relative protein levels. *Gramd1b* is transcriptionally regulated by LXR in macrophages, suggesting that Aster-B most likely plays the dominant role in responding to sterol loading. In line with this idea, our NanoSIMS imaging results showed that loss of Aster-B was sufficient to increase the PM pool of accessible cholesterol. Although the combined loss of Aster-A and Aster-B did not further increase amounts of PM accessible cholesterol, the changes in gene expression were more pronounced in the double-knockout macrophages. We did not test accessible-cholesterol levels in response to Aster-C deletion because, although it is highly expressed in some tissues, Aster-C expression is extremely low in most immortalized cell types.

The inner leaflet of the PM normally contains ∼10 mol% phosphatidylserine (14). Earlier studies showed that the GRAM domain of Aster-B is able to bind immobilized phosphatidylserine or liposomes containing high levels of phosphatidylserine (≥80 mol%) in the absence of cholesterol (7, 8). However, in living cells, Asters are recruited to the PM (where phosphatidylserine is invariably present) only in the setting of cholesterol loading (7). Our cosedimentation assays revealed that the amount of accessible cholesterol in phospholipid liposomes is a key determinant of GRAM domain binding. In contrast to ALO-D4, which binds cholesterol in phosphatidylcholine liposomes, the binding of the GRAM domain of Aster-B to cholesterol requires that liposomes contain phosphatidylserine. While our studies were in progress, Naito et al. reported findings consistent with the results presented here (8). They showed that all three Aster/Gramd1 proteins move cholesterol to the ER when the PM pool of accessible cholesterol is expanded by treating cells with sphingomyelinase. They further reported that the presence of anionic lipids, including phosphatidylserine, enhanced the binding of the Aster GRAM domain to cholesterol-containing liposomes in cosedimentation assays (8).

We hypothesize that the accumulation of accessible cholesterol in the PM alters the presentation of phosphatidylserine in the inner leaflet of the PM, thereby facilitating the binding of the Aster GRAM domain. There is an interesting precedent for this idea in the recognition of sphingomyelin by lipid-binding proteins. Endapally et al. (15) showed that ostreolysin A can distinguish between conformations of sphingomyelin, i.e., when bound to cholesterol versus when free from cholesterol. It has been suggested previously that cholesterol associated with phosphatidylserine is important for endocytosis-mediated lipid transport (16). Hirama and coworkers reported that the codistribution of PS and cholesterol in cellular membranes allows the formation of nanodomains where the headgroups of phosphatidylserine are kept separated, thus limiting spontaneous curvature of the membrane and protecting cholesterol from the aqueous medium. Our data suggest that localized plasma membrane PS and cholesterol composition may also be critical for nonvesicular cholesterol transport. Further studies will be required to understand the cholesterol-dependent GRAM domain

binding to phosphatidylserine, as well as the GRAM domain sequences that mediate binding to anionic phospholipids in the PM.

MATERIALS AND METHODS

Cell culture. 3T3-L1 cells were obtained from the American Type Culture Collection. Cell lines were previously verified by short tandem repeat profiling by ATCC and were confirmed to be mycoplasma free. Cells were grown in monolayers at 37°C in 5% CO_2 in Dulbecco's minimal Eagle medium (DMEM) containing 10% fetal bovine serum (FBS). The cholesterol-depleting medium was DMEM supplemented with LPDS. Generation 2.5 constrained ethyl ASOs were synthesized as described previously (17). A control or Aster-A ASO (GTGGAATTTATTCAGG) was used. Undifferentiated murine 3T3-L1 cells were plated in 10% FBS DMEM on day 0. On day 1, the cells were washed and supplemented with 1% LPDS. The cells were then transfected with ASOs using Dharmafect 1 reagent (Dharmacon; 50 nM final concentration) according to the manufacturer's recommendations. On day 2, the medium was changed to fresh DMEM with 1% LPDS, simvastatin (5 mM), and mevalonate (50 mM). On day 3, the cells were lifted with TrypLE, washed with DMEM plus 1% LPDS, and then plated onto silicon wafers (50,000 cells/wafer). On day 4, the cells were treated with DMEM plus 1% LPDS, simvastatin/mevalonate, and 50 μM [^{13}C]cholesterol-MβCD for 3 h.

Preparation of [^{13}C]cholesterol. [^{13}C]cholesterol was provided by Howard Riezman (University of Geneva, Geneva, Switzerland). [^{13}C]cholesterol-MβCD was prepared as described previously (10). Briefly, [^{13}C]cholesterol was dissolved in 100% ethanol to a concentration of 7.5 mg/ml and then added to 5% (wt/vol) methyl-β-cyclodextrin (Sigma) in double-distilled H_2O (ddH$_2$O) in an 80°C water bath while stirring. The MβCD/[^{13}C]cholesterol ratio was 10:1. The MβCD-[^{13}C]cholesterol solution was lyophilized, dissolved in ddH$_2$O, and filtered through a 0.22-μm filter. The concentration of [^{13}C]cholesterol in the reconstituted [^{13}C]cholesterol-MβCD complexes was 2.5 mM. The [^{13}C]cholesterol-MβCD complexes were stored at 4°C.

Mice. All mice were housed in a temperature-controlled room under a 12-h light-dark cycle under pathogen-free conditions. The mice were maintained on a standard chow diet. Experiments were performed with male mice. Aster-A global-knockout mice were generated at the Transgenic Mouse Facility at the University of California, Irvine, CA, on a C57BL/6N background using the CRISPR/Cas9 strategy outlined in Fig. 3A. CRISPR guides targeted the region between exon 2 and intron 4, resulting in a frameshift mutation caused by deletion of the targeted region between exon 2 and intron 4. Aster-B knockout mice have been previously described (7). All animal experiments were approved by the UCLA Institutional Animal Care and Research Advisory Committee. Experimental mice were sacrificed at age 8 to 12 weeks.

Mouse peritoneal-macrophage isolation and culture. Wild-type C57BL/6 mice were injected intraperitoneally with 2.5 ml of 3% Difco fluid thioglycolate medium (Becton, Dickinson). Three days later, macrophages were harvested by peritoneal lavage with 25 ml of Dulbecco's minimal Eagle medium (Corning; MT-10-013-CM). The cells were centrifuged at 400 $\times$ g for 5 min at 4° C, incubated with red blood cell lysing buffer (Sigma), and washed two times with cold DMEM. For scanning electron microscopy (SEM) and NanoSIMS studies, cells were plated onto 0.5-cm² silicon wafers in 24-well plates (200,000 cells/well). For fluorescence microscopy, cells were plated onto glass coverslips in 24-well plates (200,000 cells/well). All substrates were sterilized and coated with 0.1 mg/ml of poly-D-lysine (Sigma). For RNA, cells were plated in 6-well plates (1.5 million cells/well). Macrophages were incubated overnight in macrophage growth medium (Dulbecco's minimal Eagle medium [Corning] supplemented with 1% sodium pyruvate and 1% glutamine) containing 10% FBS (Omega Scientific). For SEM/NanoSIMS studies and for fluorescence microscopy, macrophages were switched on the following day to a medium (Dulbecco's minimal Eagle medium [Corning] supplemented with 1% sodium pyruvate and 1% glutamine) containing 1% lipoprotein-deficient bovine serum (Fisher) and 50 μg/ml acetylated low-density lipoprotein from human plasma (Ac-LDL) (Fisher). After 48 h, ^{15}N-labeled His-tagged ALO-D4 was added to the cells. For gene expression studies, the day after isolation, the cells were switched to cholesterol-depleting medium (Dulbecco's minimal Eagle medium [Corning] supplemented with 1% sodium pyruvate and 1% glutamine) containing 1% lipoprotein-deficient bovine serum (Fisher). After 24 h, the starvation medium was refreshed in the presence or absence of 50 μM cholesterol-cyclodextrin. The cells were lysed after 2 h.

Preparation of His-tagged ALO-D4 and ^{15}N-labeled His-tagged ALO-D4. A plasmid for ALO-D4 (ALO amino acids 404 to 512 with C472A and S404C substitutions) was originally obtained from Arun Radhakrishnan (University of Texas Southwestern Medical Center, Dallas, TX), and ^{15}N-labeled ALO-D4 was prepared as described previously (10) with some modifications. Briefly, ALO-D4 was expressed in *Escherichia coli* BL21(DE3) pLysS (Invitrogen). A single colony was inoculated in LB medium and grown at 37°C to reach an optical density at 600 nm (OD$_{600}$) of 0.6. One milliliter of the cell culture was added to 25 ml of minimal medium containing 20.2 mM NH$_4$Cl and 2 g of glucose and grown at 37°C to reach an OD$_{600}$ of 0.6. Next, the 25 ml of cell culture was added to 1 liter of the minimal medium and grown at 37°C to reach an OD$_{600}$ of 0.6 before it was induced with 1 mM isopropyl-β-D-1-thiogalactopyranoside (IPTG) at 18°C for 16 h. ^{15}N-labeled NH$_4$Cl was used for the production of ^{15}N-labeled ALO-D4. Cells were pelleted and lysed by douncing with a homogenizer, followed by sonication. The lysate was centrifuged at 4°C, and the supernatant was collected and mixed with 4 ml of HisPur cobalt resin (50% bed volume; ThermoFisher Scientific). The proteins were allowed to bind to the resin at 4°C for 1 h before the flowthrough was collected by loading the mixture onto a column and allowing it to flow through by gravity. The resin was washed, and ALO-D4 or ^{15}N-labeled ALO-D4 was eluted with a buffer containing 300 mM imidazole. The eluates were pooled and concentrated to 500 μl with an Amicon 10-kDa-cutoff

concentrator (Millipore) before it was further purified with a Superdex 200 gel filtration column (GE Healthcare). The purified ^{15}N-labeled ALO-D4 was concentrated to 1 ml and stored at 4°C.

NanoSIMS analysis. For NanoSIMS studies, fibroblasts and macrophages were processed as described previously (10). Briefly, the cells were fixed with 2.5% glutaraldehyde (Electron Microscopy Sciences) and 4% paraformaldehyde (PFA) (Electron Microscopy Sciences) in 0.1 M phosphate buffer (pH 7.4) for 20 min at 4°C and then 1 h at room temperature. Each 100 ml of 0.1 M phosphate buffer contained 1.14 g NaH_2PO_4 and 1.69 g Na_2HPO_4. The cells were washed and then postfixed with 1% osmium tetroxide (Electron Microscopy Sciences) in 0.1 M phosphate buffer for 45 min, washed, and air dried. Samples were coated with a 4-nm thickness of iridium using an ion beam sputtering system (South Bay Technologies). A NanoSIMS 50L instrument (Cameca) was used to analyze samples. A focused ^{133}Cs$^+$ primary beam bombarded the iridium-coated cells and released secondary ions (^{12}C$^-$, ^{13}C$^-$, ^{16}O$^-$,^{14}N^{12}C$^-$, ^{15}N^{12}C$^-$, ^{31}P$^-$, and ^{32}S$^-$) and secondary electrons (SE), which were collected and quantified. For Fig. 2, a 1-nA beam current (primary aperture D1 = 1) was used to scan an area of 50 μm by 50 μm with a dwell time of 100 μs/pixel and scans of 256 by 256 for 25 s to implant ^{133}Cs$^+$. In the same area, a 45-μm-by-45-μm image was obtained with a 2.5-pA beam current (primary aperture D1 = 2), a dwell time of 1 ms/pixel, and one frame of 512 by 512 pixels. For Fig. 4 and 5, NanoSIMS images (45 μm by 45 μm) were obtained with a 4-pA beam current (primary aperture D1 = 2), a dwell time of 0.15 ms/pixel, and 4 frames of 1,024 by 1,024 pixels.

To quantify ^{13}C/^{12}C and ^{15}N/^{14}N ratios in fibroblasts and ^{15}N/^{14}N ratios in macrophages, we selected whole cells with ^{12}C^{14}N$^-$ NanoSIMS images, and regions of interest were defined with the OpenMIMS plugin in ImageJ. The mean ^{15}N/^{14}N and ^{13}C/^{12}C ratios of each fibroblast and the mean ^{15}N/^{14}N ratio of each macrophage were measured and processed with Prism 7.0. Differences were assessed by a Student t test with Welch's correction.

Preparation of fluorescent ALO-D4 and ^{15}N-labeled ALO-D4. Purified protein was conjugated as described previously (11) with slight modifications. Briefly, ALO-D4 or ^{15}N-labeled ALO-D4 with cysteine substituted was incubated with Alexa Fluor 594 (Life Technologies) at 4°C overnight in 50 mM Tris-HCl (pH 7.5) and 150 mM NaCl (1× Tris-buffered saline [TBS]) containing 1 mM Tris(2-carboxyethyl)phosphine hydrochloride (TCEP). Free dye was separated by extensive buffer exchange with 1× TBS in an Amicon 10-kDa-cutoff concentrator (Millipore) and stored at 4°C.

Binding of ALO-D4 to cells. Cells were incubated with ALO-D4 as described previously (10). Briefly, macrophages were washed three times for 10 min each time in phosphate-buffered saline (PBS)-Ca^{2+}-Mg^{2+} (Life Technologies) containing 0.2% (wt/vol) bovine serum albumin (BSA). The cells were then incubated with ALO-D4 in PBS-Ca^{2+}-Mg^{2+} containing 0.2% (wt/vol) BSA for 2 h at 4°C. Unbound proteins were removed by washing with PBS-Ca^{2+}-Mg^{2+} three times for 2 min each time.

Confocal-microscopy analysis. After binding of fluorescently labeled ALO-D4, the cells were fixed with 3% paraformaldehyde for 15 min, stained with 5 μg/ml DAPI (4′,6-diamidino-2-phenylindole), and then washed twice with PBS-Ca^{2+}-Mg^{2+} for imaging. Images were taken with an Axiovert 200M microscope and processed with Zen 2010 software (Zeiss).

Quantification of fluorescence intensity. For signal quantification, cells were plated on 24-well plates (Cellvis; P24-0-N), treated, stained as described above, fixed in Dulbecco's PBS (DPBS)-Ca^{2+}-Mg^{2+}, and imaged within 2 h. The images were taken at the UCLA Molecular Screening Shared Resource core facility on a Molecular Devices ImageXpress confocal microscope using a 20× objective (Nikon Plan Fluor; 0.3 numerical aperture [NA]) with Molecular Devices ImageXpress XL. The maximum projected cellular fluorescence intensity was assessed with MetaXpress software with Powerscore using the multiwavelength cell-scoring module. Integrated fluorescence intensity profiles were exported and analyzed using R with the ggplot2 package (18). Differences were assessed by Student's t test with Welch's correction.

Gene expression analysis. Total RNA was isolated using TRIzol reagent (Invitrogen) and reverse transcribed with an iScript cDNA synthesis kit (Bio-Rad). cDNA was quantified by real-time PCR using SYBR green master mix (Bio-Rad) on an ABI 7900 instrument. Gene expression levels were determined by using a standard curve. Each gene was normalized to the housekeeping gene 36B4 and was analyzed in duplicate. The primers used for real-time PCR are available upon request.

Preparation of the Aster-B GRAM domain and testing its binding to liposomes. Expression vectors for the Aster-B$_{43-189}$ GRAM domain containing an N-terminal glutathione S-transferase (GST) tag were transformed into DE3 Rosetta 2 cells (Novagen). Bacterial cultures were grown at 37°C to an A_{600} of 0.6 to 0.8. Protein expression was then induced with 0.5 mM IPTG, and the cells were grown for an additional 16 h at 18°C with constant shaking. The cultures were spun down, resuspended in 30 ml of lysis buffer (PBS containing 0.5 mM dithiothreitol and a Roche Complete EDTA-free protease inhibitor tablet), and sonicated for 30 min to lyse the cells. The solution was spun down at 1,800 rpm for 30 min, and the proteins in the supernatant were incubated with a glutathione-agarose resin (Pierce; PI16100) overnight at 4°C with shaking. The bound protein was washed twice with lysis buffer and then eluted with a buffer containing 50 mM Tris, 150 mM NaCl, 10 mM reduced glutathione (pH 8.0).

Liposomes were prepared as described previously (12) with minor modifications. POPC (1-palmitoyl-2-oleoyl-glycero-3-phosphocholine) (Avanti; 850457), cholesterol (Sigma; C8667), L-α-phosphatidylserine (Avanti; 840032C; porcine brain), and/or POPE (1-palmitoyl-2-oleoyl-sn-glycero-3-phosphoethanolamine) (Avanti; 850757C) dissolved in chloroform (1,600 μM total lipid) was dried under liquid nitrogen and stored under vacuum for 3 h. Lipids dissolved in chloroform (1,600 μM total lipid) were dried under liquid nitrogen and stored under vacuum for 3 h. The lipids were resuspended in 500 μl of assay buffer (150 mM NaCl and 50 mM Tris-HCl, pH 7.5) and vortexed vigorously for 30 min at room temperature. The lipid suspensions were snap frozen in liquid nitrogen for 1 min, followed by cooling in a room

temperature water bath for 3 min (five cycles). The suspension was then sonicated for 15 min in a 37°C water bath, followed by cooling at room temperature for 15 min (2 cycles). Liposomes were pelleted at 60,000 × *g* for 45 min, resuspended in ice-cold assay buffer, and used immediately.

For liposome binding assays, 100 ng of either the Aster-B GRAM domain or ALO-D4 was incubated with 200 μl of liposomes (640 μM total lipid) for 1 h at room temperature. Liposome-bound protein (pellet [P]) was pelleted from unbound protein (supernatant [S]) in the supernatant by ultracentrifugation at 100,000 × *g* for 20 min at 4°C and then resuspended in 200 μl of the assay buffer. Equal amounts of the supernatants and resuspended pellets were subjected to immunoblot analysis with an anti-GST antibody (ThermoFisher; 1HCLC; 710011) or an anti-His tag antibody (Cell Signaling Technology; 27E8; 2366) (to detect the Aster-B GRAM domain or ALOD4, respectively).

ACKNOWLEDGMENTS

REFERENCES

1. Das A, Brown MS, Anderson DD, Goldstein JL, Radhakrishnan A. 2014. Three pools of plasma membrane cholesterol and their relation to cholesterol homeostasis. Elife 3:e02882. https://doi.org/10.7554/eLife.02882.

2. Infante RE, Radhakrishnan A. 2017. Continuous transport of a small fraction of plasma membrane cholesterol to endoplasmic reticulum regulates total cellular cholesterol. Elife 6:e25466. https://doi.org/10.7554/eLife.25466.

3. Brown MS, Goldstein JL. 1986. A receptor-mediated pathway for cholesterol homeostasis. Science 232:34–47. https://doi.org/10.1126/science.3513311.

4. Phillips MJ, Voeltz GK. 2016. Structure and function of ER membrane contact sites with other organelles. Nat Rev Mol Cell Biol 17:69–82. https://doi.org/10.1038/nrm.2015.8.

5. Antonny B, Bigay J, Mesmin B. 2018. The oxysterol-binding protein cycle: burning off PI(4)P to transport cholesterol. Annu Rev Biochem 87:809–837. https://doi.org/10.1146/annurev-biochem-061516-044924.

6. Luo J, Jiang L-Y, Yang H, Song B-L. 2019. Intracellular cholesterol transport by sterol transfer proteins at membrane contact sites. Trends Biochem Sci 44:273–292. https://doi.org/10.1016/j.tibs.2018.10.001.

7. Sandhu J, Li S, Fairall L, Pfisterer SG, Gurnett JE, Xiao X, Weston TA, Vashi D, Ferrari A, Orozco JL, Hartman CL, Strugatsky D, Lee SD, He C, Hong C, Jiang H, Bentolila LA, Gatta AT, Levine TP, Ferng A, Lee R, Ford DA, Young SG, Ikonen E, Schwabe JWR, Tontonoz P. 2018. Aster proteins facilitate nonvesicular plasma membrane to ER cholesterol transport in mammalian cells. Cell 175:514–529.e20. https://doi.org/10.1016/j.cell.2018.08.033.

8. Naito T, Ercan B, Krshnan L, Triebl A, Koh DHZ, Wei F-Y, Tomizawa K, Torta FT, Wenk MR, Saheki Y. 2019. Movement of accessible plasma membrane cholesterol by the GRAMD1 lipid transfer protein complex. Elife 8:e51401. https://doi.org/10.7554/eLife.51401.

9. He C, Hu X, Jung RS, Weston TA, Sandoval NP, Tontonoz P, Kilburn MR, Fong LG, Young SG, Jiang H. 2017. High-resolution imaging and quantification of plasma membrane cholesterol by NanoSIMS. Proc Natl Acad Sci U S A 114:2000–2005. https://doi.org/10.1073/pnas.1621432114.

10. He C, Hu X, Weston TA, Jung RS, Sandhu J, Huang S, Heizer P, Kim J, Ellison R, Xu J, Kilburn M, Bensinger SJ, Riezman H, Tontonoz P, Fong LG, Jiang H, Young SG. 2018. Macrophages release plasma membrane-derived particles rich in accessible cholesterol. Proc Natl Acad Sci U S A 115:E8499–E8508. https://doi.org/10.1073/pnas.1810724115.

11. Hu X, Weston TA, He C, Jung RS, Heizer PJ, Young BD, Tu Y, Tontonoz P, Wohlschlegel JA, Jiang H, Young SG, Fong LG. 2019. Release of cholesterol-rich particles from the macrophage plasma membrane during movement of filopodia and lamellipodia. Elife 8:e50231. https://doi.org/10.7554/eLife.50231.

12. Gay A, Rye D, Radhakrishnan A. 2015. Switch-like responses of two cholesterol sensors do not require protein oligomerization in membranes. Biophys J 108:1459–1469. https://doi.org/10.1016/j.bpj.2015.02.008.

13. Goldstein JL, Ho YK, Basu SK, Brown MS. 1979. Binding site on macrophages that mediates uptake and degradation of acetylated low density lipoprotein, producing massive cholesterol deposition. Proc Natl Acad Sci U S A 76:333–337. https://doi.org/10.1073/pnas.76.1.333.

14. Leventis PA, Grinstein S. 2010. The distribution and function of phosphatidylserine in cellular membranes. Annu Rev Biophys 39:407–427. https://doi.org/10.1146/annurev.biophys.093008.131234.

15. Endapally S, Frias D, Grzemska M, Gay A, Tomchick DR, Radhakrishnan A. 2019. Molecular discrimination between two conformations of sphingomyelin in plasma membranes. Cell 176:1040–1053.e17. https://doi.org/10.1016/j.cell.2018.12.042.

16. Hirama T, Lu SM, Kay JG, Maekawa M, Kozlov MM, Grinstein S, Fairn GD. 2017. Membrane curvature induced by proximity of anionic phospholipids can initiate endocytosis. Nat Commun 8:1393. https://doi.org/10.1038/s41467-017-01554-9.

17. Seth PP, Siwkowski A, Allerson CR, Vasquez G, Lee S, Prakash TP, Wancewicz EV, Witchell D, Swayze EE. 2009. Short antisense oligonucleotides with novel 2′−4′ conformationaly [sic] restricted nucleoside analogues show improved potency without increased toxicity in animals. J Med Chem 52:10–13. https://doi.org/10.1021/jm801294h.

18. Wickham H. 2016. ggplot2: elegant graphics for data analysis, 2nd ed. Springer, New York, NY. https://doi.org/10.1007/978-3-319-24277-4_5.